NEOPLASIA
www.neoplasia.com

Volume 10 Number 3 March 2008 pp. 207–216 207

Cellular Magnetic Resonance Imaging: *In Vivo* Imaging of Melanoma Cells in Lymph Nodes of Mice[1]

Paula J. Foster*,†, Elizabeth A. Dunn†, Kristina E. Karl‡, Jonatan A. Snir*,†, Colleen M. Nycz‡, Alfred J. Harvey‡ and Ron J. Pettis‡

*Imaging Research Laboratories, Robarts Research Institute, London, ON, Canada; †Department of Medical Biophysics, University of Western Ontario, London, ON, Canada; ‡Becton Dickinson Technologies, Durham, NC, USA

Abstract

Metastasis is responsible for most deaths due to malignant melanoma. The clinical significance of micrometastases in the lymph is a hotly debated topic, but an improved understanding of the lymphatic spread of cancer remains important for improving cancer survival. Cellular magnetic resonance imaging (MRI) is a newly emerging field of imaging research that is expected to have a large impact on cancer research. In this study, we demonstrate the cellular MRI technology required to reliably image the lymphatic system in mice and to detect iron-labeled metastatic melanoma cells within the mouse lymph nodes. Melanoma cells were implanted directly into the inguinal lymph nodes in mice, and micro-MRI was performed using a customized 1.5-T clinical MRI system. We show cell detection of as few as 100 iron-labeled cells within the lymph node, with injections of larger cell numbers producing increasingly obvious regions of signal void. In addition, we show that cellular MRI allows monitoring of the fate of these cells over time as they develop into intranodal tumors. This technology will allow noninvasive investigations of cellular events in cancer metastasis within an entire animal and will facilitate progress in understanding the mechanisms of metastasis within the lymphatic system.

Neoplasia (2008) 10, 207–216

Introduction

Melanoma is a form of skin cancer with 160,000 new cases reported annually worldwide [1]. It is diagnosed most frequently in Caucasian males and is particularly common in populations living in sunny climates [2]. According to a World Health Organization report, approximately 48,000 deaths due to malignant melanoma are registered annually [3]. Most of these deaths are due to metastatic infiltration of distant organ tissues [4].

When staging melanoma, the critical question is whether tumor cells have metastasized to other tissues. For localized disease, surgical resection of the primary tumor before it achieves a thickness of more than 1 mm is generally a very successful therapy [5]. If the melanoma has spread to the lymph nodes, then the most predictive factor is the number of tumor-positive nodes [6]. The extent of malignancy within a node is also important; metastases in which malignancy is only microscopic have a more favorable prognosis than macrometastases [7]. However, once the disease has metastasized beyond the nodes to distant organ tissues, the cancer is generally considered incurable, and a 5-year survival rate is less than 10% [8].

Cancer metastasizes through a series of sequential, interrelated steps, each of which is rate limiting [9]. These include: 1) invasion of cancer cells into the lymph vessels or bloodstream or delivery to organs, such as the lymph nodes, liver, lung, bone, or brain; 2) extravasation of cells into the organ parenchyma; 3) cell proliferation to form secondary (late-stage) tumors; and 4) development of new blood vessels to sustain continued growth. Despite many years of laboratory and clinical research, late-stage melanoma treatments have not been very successful. Therefore, a noninvasive method to detect and screen for earlier and smaller lymph-node micrometastases may greatly reduce the mortality rate associated with melanoma.

Address all correspondence to: Dr. Paula J. Foster, Imaging Research Laboratories, Robarts Research Institute, 100 Perth Drive, London, Ontario, Canada N6A 5K8.
E-mail: pfoster@imaging.robarts.ca

[1]Financial Support for P.J.F.: Canadian Health Institute of Research Grant#MOP-79547, RBC Financial.
Received 29 October 2007; Revised 6 December 2007; Accepted 10 December 2007

DOI 10.1593/neo.07937

To study melanoma, metastastic mouse models have been developed using both mouse-derived and human-derived melanoma cell lines [10–12]. Preclinical models are typically characterized by gross lesion description and histology. Unfortunately, all of these methods are invasive and require that animals be sacrificed to collect the data, prohibiting longitudinal measurements in the same animal. Sensitive and specific noninvasive imaging techniques are key to gaining information about the fate of cancer cells and metastasis *in vivo*.

A number of *in vivo* imaging modalities can assess tumor development in preclinical animal models. These include optical techniques, such as bioluminescence imaging [13] and intravital video microscopy [14], computed tomography [15], ultrasound (US) [16], nuclear imaging techniques, such as positron emission tomography [17] and single-photon emission computed tomography [18], and magnetic resonance imaging (MRI) [19].

High-resolution MRI provides an exceptional imaging modality for studying tumor progression. Magnetic resonance imaging can provide three-dimensional (3D), detailed anatomic information in a noninvasive manner, with current micro-MRI techniques capable of *in vivo* resolution on the order of tens of micrometers [20,21]. Unlike histologic analyses, which provide only a *snapshot* of the overall process, MRI can provide a dynamic view of disease progression, delivers results in real time, requires fewer animals, and is free from sectioning-related artifacts. Thus, MRI may provide a more complete picture of the overall biologic process under investigation.

Cellular MRI is a young field of imaging research that combines the high resolution of micro-MRI with sensitive iron oxide–based contrast agents for cell and receptor labeling [22,23]. This combination allows for the investigation of biologic processes at the cellular level. The presence of this magnetic label in cells causes a distortion in the magnetic field and leads to signal hypointensities (negative contrast) in MR images [24]. The development of a broad range of iron oxide contrast agents, as well as cell labeling techniques [25–28], has stimulated the development of a range of applications for MRI cell tracking. A variety of iron oxide–based labels are available including superparamagnetic iron oxide particles (SPIO), ultrasmall iron oxide agents (USPIO) and micrometer-sized iron oxide particles (MPIO). Micrometer-sized iron oxide particles have advantages over SPIO or USPIO for labeling cancer cells. Micrometer-sized iron oxide particles contain more iron and offer the possibility of greatly increasing iron content in labeled cells. The polymer coating of MPIO should be inert to the cell, allowing long-term studies of labeled cells and their progeny [29]. Cancer cells take up MPIO rapidly and efficiently and, even at high iron loadings, are not toxic or known to adversely affect cancer cell function [30]. In addition, MPIO can be purchased with a fluorophore that allows for correlative microscopy.

Cellular MRI offers the opportunity for early detection of small numbers of metastatic cells and also provides the opportunity for studying micrometastatic processes in their earliest developmental stages in the target organs of interest. In this study, we demonstrate that cellular MRI can be used to reliably image the lymphatic system in mice and to detect iron-labeled metastatic melanoma cells within the mouse lymph nodes.

Materials and Methods

Cell Culture and MPIO Labeling

Murine B16F10 melanoma cells were chosen because of their high metastatic potential to regional lymph nodes [31]. B16F10 melanoma cells were maintained in Dulbecco's modified Eagle's medium–high glucose media (Invitrogen, Ontario, Canada) containing 10% FBS at 37°C and 5% CO_2. For MPIO labeling, 5×10^5 cells were plated in six-well dishes, supplemented with media and allowed to adhere for 24 hours. MPIO beads, 5.0×10^8 (0.9 μm in diameter, ~63% magnetite) (Bangs Laboratories, Fishers, IN), were added to 2 ml of media in each well of a six-well dish, and cells were incubated for an additional 24 hours. Cells were washed thoroughly with PBS to remove unincorporated MPIO, and cell viability was assessed using Trypan blue exclusion. To quantify the extent of MPIO labeling, 2×10^6 cells were suspended in gelatin and aliquoted into microcentrifuge tubes for the quantification of cellular iron uptake. The mean cellular MPIO content, expressed in picogram of Fe per cell, was assessed by inductively coupled plasma–mass spectroscopy (ICP-MS).

To monitor the iron concentration in dividing cells, 1 million B16F10 cells were added to 50-ml tissue culture flasks and allowed to adhere and propagate. A day after plating, while cells were in logarithmic growth, MPIO were added to the media of half the flasks, whereas other flasks remained unlabeled as controls. Cells were incubated with the label for 24 hours then harvested, washed, and counted. Aliquots of cells from both groups were collected for iron quantification by ICP-MS and for visualization of beads under the microscope. One million labeled or unlabeled cells were then replated and allowed to propagate further. Cells were collected for quantification and further subcultured on days 3, 5, 10, and 13 postlabeling.

Animal Model

To standardize the probability of tumor development and cellular burden in the lymph node, cells were injected directly into the inguinal lymph node of female C57Bl/6 mice (17 to 20 g) (Charles River Laboratories, Wilmington, MA). Mice were cared for in accordance with the standards of the Canadian Council on Animal Care and under an approved protocol of the University of Western Ontario's Council on Animal Care. A superficial skin incision, approximately 1 cm in length, was made in the lower right abdominal quadrant of anesthetized mice. The skin was inverted to expose the right inguinal lymph node. A 5-μl volume of B16F10 cells was then slowly injected using a Hamilton syringe and an investigational microneedle (BD, Franklin Lakes, NJ). The dermal incision was closed with VetBond Tissue Adhesive (3M, St. Paul, MN). Mice received either 100 (n = 5), 1000 (n = 10), or 10,000 MPIO-labeled cells (n = 20). Control groups received saline (n = 2) or unlabeled cells (10,000, n = 3).

Magnetic Resonance Imaging

All MRI scans was performed on a 1.5-T GE CV/i whole-body clinical MR scanner (General Electric, Mississauga, Canada) using a custom-built gradient coil (inner diameter, 17.5 cm; maximum gradient strength, 500 mT/m; and peak slew rate, 3000 T/m per second) and a custom-built solenoidal mouse body radiofrequency coil. The radiofrequency coil was built to permit the simultaneous imaging of inguinal, popliteal, and axial lymph nodes, and it had a diameter of 4 cm and a length of 4.5 cm. Mice were anesthetized with isofluorane (1% in 100% oxygen) using a nose cone with vacuum for scavenging. *In vivo* images were obtained using a 3D balanced steady-state free precession imaging sequence [Fast Imaging Employing Steady State Acquisition (FIESTA) on the GE system]. A number of sequence parameters were optimized to achieve high-quality, mouse whole-body images including the bandwidth (BW), repetition time (T_R), echo time (T_E), and flip angle. The optimized sequence employed T_R/T_E = 9.1/4.5 milliseconds, flip angle = 30°, BW = ±21 kHz, two signal averages, and phase cycling.

Images were acquired at either 200-μm^3 isotropic spatial resolution with two signal averages (34 minutes) or at 100-μm^3 isotropic spatial resolution with eight signal averages (68 minutes). Zero filling was used to give an interpolated voxel dimension of 120 × 120 in-plane.

Two imaging experiments were performed: a longitudinal study and a cross-sectional study. In the longitudinal study, mice were injected with different numbers of labeled cells (100 cells, n = 5; 1000 cells, n = 10; 10,000 cells, n = 5) imaged repeatedly on days 1, 4, 7, 14, and 22 postinjection and then sacrificed for histological analysis. In the cross-sectional study, five groups of three mice (total, n = 15) were injected with 10,000 labeled cells, and the separate groups of mice were imaged once at five different time points (days 1, 8, 10, 12, and 15) and then sacrificed for histological analysis.

Image Processing

During the imaging optimization steps, image quality was measured by calculating the node signal-to-noise ratio (SNR) and the contrast-to-noise ratio between the lymph node and the fat. The average contrast from regions of signal loss was measured using an image analysis package (ImageJ; National Institutes of Health, Bethesda, MD). Signal void contrast was expressed as the percent signal drop compared to background node tissue and was calculated by taking the signal difference between background node tissue and a region of interest within the region of signal loss, dividing by the background signal, and multiplying this fractional signal loss by 100%. The number and size of lymph node and tumors were measured using another image analysis package (VG Studio Max, Heidelberg, Germany).

Histology

Lymph nodes and tumors were removed at the end of the experiment and fixed in 10% buffered formalin. Paraffin-embedded lymph nodes and tumors were sectioned at 10-μm thickness. Staining methods included hematoxylin and eosin (H&E) to visualize tumor and node morphology, S100 (polyclonal antibody, Z311; Dako, Ontario, Canada) to identify melanoma cells, and Perls' Prussian blue (PPB) staining to visualize iron.

Results

In Vivo *MRI of Mouse Lymph Nodes*

Figure 1 shows representative *in vivo* coronal FIESTA image slices through the mouse body in a control mouse that did not receive any injection. The image resolution is 200 μm in each of the three dimensions. In these data sets, the axillary, inguinal, and popliteal lymph nodes can all be readily visualized, although not all in the same image slice. At least 10 different lymph nodes could be easily identified in the FIESTA images.

The normal lymph nodes are clearly visualized as structures within the fat pad, due to the very high contrast between the normal node and the surrounding fat; the mean fat–node contrast-to-noise ratio measured for normal lymph nodes (n = 10) was 72. The mean inguinal node SNR was 35. The volumes of the normal axillary, inguinal, and popliteal lymph nodes were measured to be 3.54 (±0.31), 3.20 (±0.81), and 0.79 (±0.36) mm^3, respectively.

Part of the FIESTA sequence optimization involved varying the receiver bandwidth and timing parameters. As the BW in the FIESTA imaging sequence is changed, the T_R/T_E changes. With spatial resolution held at 100 × 100 × 200 m^3, varying the BW between ±16 and ±41 kHz produces T_R/T_E values of 9.0/4.5 to 4.0/2.3 milliseconds, respectively. Increasing the BW (shorter timing parameters T_R/T_E) will reduce the scan time but will also reduce the SNR. In addition, the shorter T_E reduces the contrast generated by iron-labeled cells. The choice of BW for live mouse imaging must consider all of these factors. The optimal BW and timing parameters, for mouse body FIESTA imaging, were determined to be ±21 kHz with T_R/T_E of 9.1/4.5 milliseconds.

Phase cycling was used to minimize banding artifacts that are produced with the FIESTA imaging sequence and appear as unwanted regions of low signal intensity or shadowing near tissue interfaces. Images of a control mouse, which did not receive any injection, depicting the effect of employing phase cycling are shown in Figure 2. Without phase cycling, significant banding artifacts are produced in

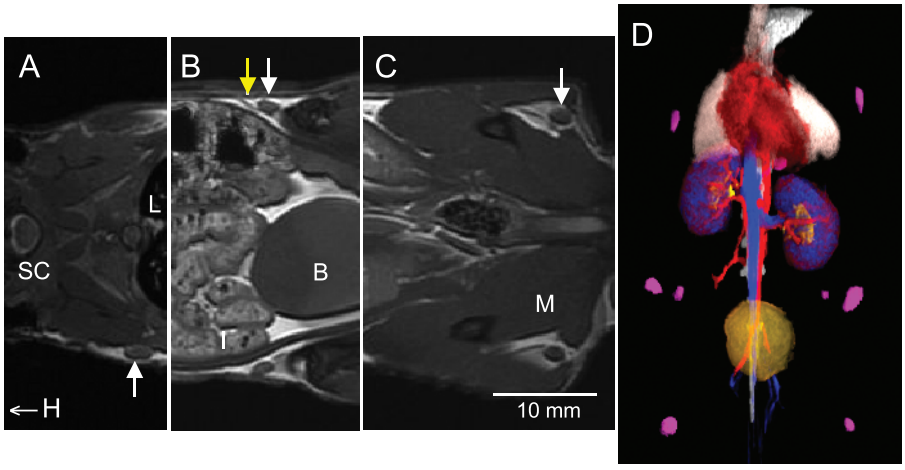

Figure 1. *In vivo* FIESTA images of the mouse body obtained with 200 × 200 × 200 μm^3 spatial resolution and a 34-minute scan time. (A–C) Three coronal FIESTA image slices are shown (cropped) from the same 3D data set and the same animal. Different lymph nodes appear in different MR slices. (A) Right axillary node (arrow). *H* indicates the direction of head; *L*, lung; *SC*, spinal cord. (B) Both inguinal nodes (white arrows) and a lymphatic vessel (yellow arrow). *B* indicates the bladder; *I*, intestines. (C) Both popliteal nodes (white arrows). *M* indicates the muscle. (D) At least 10 different lymph nodes could be easily identified in the FIESTA images. These 3D images can be rendered for easy visualization of lymph nodes of interest in the mouse, making it possible to survey the lymphatic system for cancer cells. In this rendering, the nodes are purple, the heart is red, lungs are white, the kidneys are blue, and the bladder is yellow.

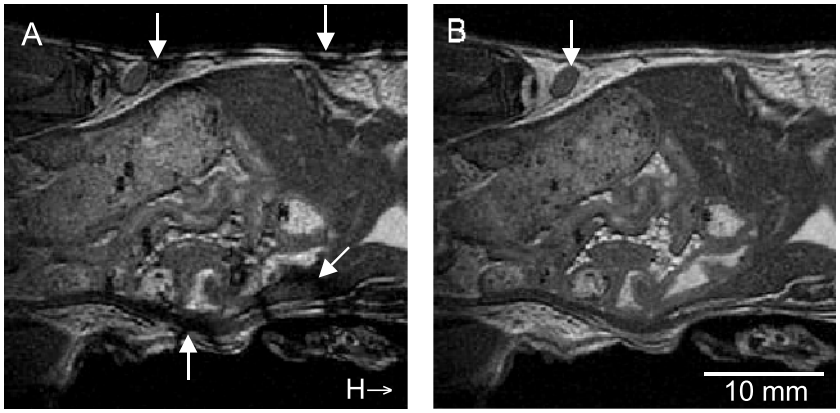

Figure 2. Coronal *in vivo* FIESTA images of a normal mouse body (no cells injected) acquired with and without radiofrequency phase cycling. (A) Phase cycling is not used. Significant banding artifacts are produced in the mouse body at existing tissue interfaces (arrows). (B) The ability to visualize the inguinal lymph node (arrow) is improved dramatically with phase cycling implemented. H indicates the direction of the mouse head.

the mouse body where many different tissue interfaces exist (Figure 2*A*, *arrows*). Banding at the body surface is especially detrimental to imaging of lymph nodes because superficial nodes are typically adherent to the skin's surface. With phase cycling implemented, the ability to visualize the inguinal lymph node (*arrow*) is improved dramatically (Figure 2*B*).

B16F10 Cell Labeling

B16F10 cells readily take up the MPIO label while maintaining high viability. The labeling efficiency was 100%; however, the extent of iron labeling per cell varied (Figure 3*B*). Standard methods for measuring iron content provide only the average amount of iron per cell; the mean iron loading, measured by ICP-MS, was 35 pg of Fe/cell. The doubling time of both the MPIO-labeled and unlabeled cells was equivalent at approximately 20 hours. Trypan blue staining revealed no difference in cell viability for MPIO-labeled cells *versus* unlabeled cells (not shown). The serial photomicrographs in Figure 3*B* show the presence of the beads (unstained, brown) in B16F10 cells and demonstrate the disappearance of intracellular iron from the rapidly dividing cells. There appeared to be a complete loss of detectable iron by day 5, corresponding to the sixth generation of daughter cells. Iron content analysis by ICP-MS was consistent with microscopy results also revealing the reduction of cellular iron to background levels (Figure 3*A*).

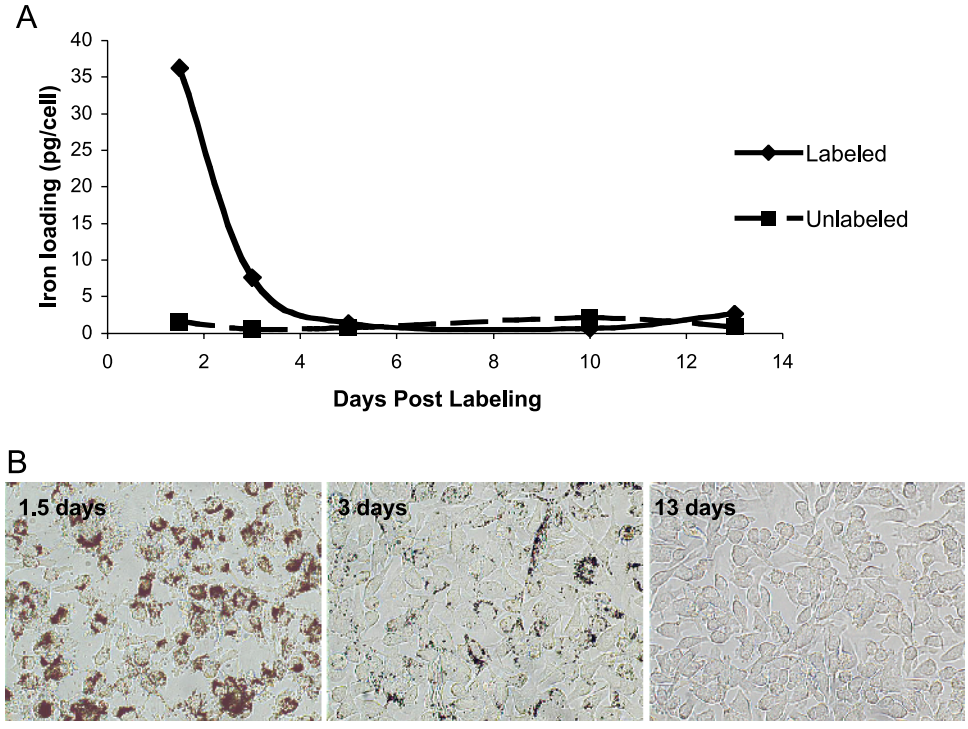

Figure 3. (A) Iron content measurements by ICP-MS and (B) photomicrographs of unstained MPIO-labeled B16F10 cells show the rapid disappearance of iron in dividing cells.

The microinjection of cells into the inguinal lymph node did not adversely affect the cell viability or alter the observed nodal structure. This is confirmed by the finding of 95 ± 4.4% cell viability after the passage of cells through the microneedle system. In addition, we have observed proper lymphatic flow into and out of the node, 24 hours following the cell injection, using Evan's blue dye (data not shown).

In Vivo *MRI of MPIO Labeled Melanoma Cells: Longitudinal Imaging*

MRI appearance of labeled cells. MPIO-labeled melanoma cells appeared as regions of signal loss in FIESTA images of the injected inguinal nodes. In Figure 4, MR images of the inguinal lymph nodes, on day 1 postinjection, are shown cropped and enlarged: (*A*) saline injection, (*B*) 100 cells, (*C*) 1000 cells, and (*D*) 10,000 cells. These images were acquired in the coronal plane at a spatial resolution of 200 μm^3. Blinded observers could not routinely distinguish between images of lymph nodes injected with saline and lymph nodes injected with 100 MPIO-labeled cells. Distinct regions of signal loss were consistently observed within lymph nodes injected with 1000 cells, and the region of signal loss was further increased in the lymph nodes injected with 10,000 cells. This was expected because the MPIO within the cell affects the MR signal over a large volume surrounding the cell, i.e., a so-called *blooming effect*.

In a subsequent group of mice injected with 100 cells (n = 5), images were acquired in the axial plane with a higher spatial resolution and a longer scan time. Figure 5 shows that in these images, with 100-μm^3 spatial resolution, small focal patterns of signal loss could be observed. This observation was made in fours (80%) of five mice injected with 100 MPIO-labeled melanoma cells, and the signal loss persisted for 22 days postinjection. Figure 5*C* shows that PPB-positive cells are present in the implanted node at day 22. These cells appear to be located mainly in the center of the node. Some cells can be detected that are positive for both iron and melanin (Figure 5*D*). Signal loss was not observed in nodes that were not injected with cells or in nodes injected with saline or unlabeled cells (not shown).

Tumor development. Tumor growth could be detected in the MR images, on day 14 postinjection, in 5 of the 10 mice injected with 1000 cells. In the five mice injected with 10,000 cells, tumors were visualized in two by day 7 and in all by day 14. Tumor growth was not observed with MRI in mice injected with 100 cells. The evolution of tumor growth was monitored using MRI, and Figure 6 shows representative time course FIESTA images of mice injected with 1000 (Figure 6*A*) or 10,000 (Figure 6*B*) MPIO-labeled melanoma cells. In Figure 6*A*, the spatial distribution of the signal loss within the node appears similar over time as the tumor grows, but morphologic changes in nodal structure are observed as early as day 4 postinjection. On day 1, at the higher 10,000-cell load (Figure 6*B*), there is a greater blooming artifact, likely due to the larger number of cells, and therefore, iron in the sample. Morphologic changes remain visible early on, and on equivalent days, the tumors are consistently larger than those in the 1000-cell cohort. The appearance of tumors in this group was similar in all mice with signal loss becoming dispersed throughout the tumor tissue over time, with a multilobular structure and signal hyperintensity (brightness) appearing by day 22.

In Vivo *MRI of MPIO Labeled Melanoma Cells: Cross-Sectional Study*

In mice imaged at day 1 postinjection, signal loss was observed in the nodes of the three mice injected at the 10,000-cell load. In each case, this appeared as a large region of signal loss at the inguinal node that partially or completely interfered with visualization of the node itself. These results were consistent with, and predicted by, the observations of mice from the previous longitudinal experiment. In mice sacrificed at day 1 postinjection, no pigmentation was observed. In mice imaged on day 8 postinjection, signal loss was again observed in all (three) animals. At sacrifice, a small focal region of pigmentation was typically observed in the excised tissue.

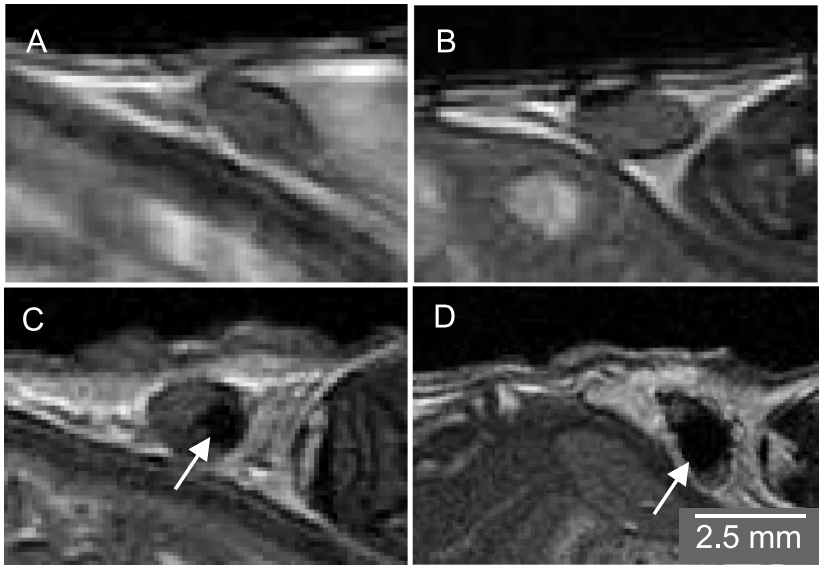

Figure 4. Coronal *in vivo* FIESTA images of mouse inguinal lymph nodes acquired with 200 × 200 × 200 μm^3 spatial resolution in 34 minutes (cropped and enlarged). Images were acquired on day 1 postinjection of (A) saline, (B) 100 MPIO-labeled cells, (C) 1000 MPIO-labeled cells, and (D) 10,000 MPIO-labeled cells. Regions of signal loss are apparent in C and D (arrows).

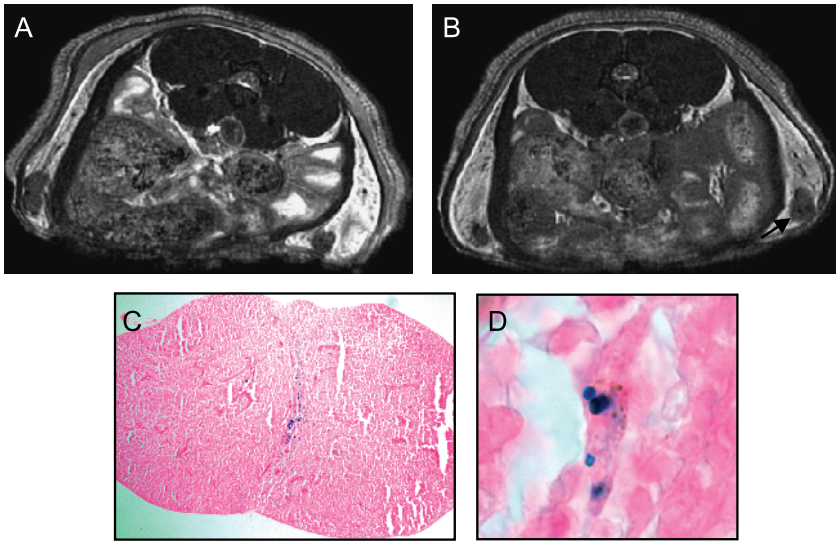

Figure 5. Axial *in vivo* FIESTA images of the inguinal lymph nodes of a mouse acquired with 100 × 100 × 100 μm^3 spatial resolution in 68 minutes. The mouse was injected with 100 MPIO-labeled cells, and the images were acquired on (A) days 4 and (B) 22 postinjection. Small focal regions of signal loss within the node persist over this time course. No tumor growth was evident at dissection. (C) PPB staining (original magnification, ×40) of this node at day 22 shows the existence of iron-positive cells. (D) At higher magnification (×100), cells that are PPB-positive and have brown pigmentation, which indicates melanin, can be identified.

In mice imaged on day 10 postinjection, the MR scan's appearance was more variable. Signal loss was only observed in two of three mice. In these mice, the node appeared enlarged, tumor growth was evident, and signal loss was dispersed throughout the tumor. At dissection, the nodes appeared up to twice the normal size, and the exterior was darkly pigmented. In the one mouse that did not show signal loss in the node, the node appeared normal in size and color at dissection.

The MR scan's appearance of mice imaged on day 12 postinjection was also variable. Signal loss was observed in all three mice. In one mouse, a large tumor was obvious at the node. The signal loss was dispersed throughout the node, and at dissection, the tumor was approximately four times the size of the normal node and darkly pigmented. In two of three mice, signal loss was observed in the images but the nodes appeared normal in size. At dissection, the nodes appeared normal in size and pigmented. Large tumors were obvious in the images of mice on days 15 and 22 postinjection. Signal loss was observed in all mice and was dispersed throughout the tumor. Nodes dissected at days 15 and 22 after the cell injection showed obvious tumor growth with variable pigmentation.

Figure 7 shows representative images of mice at days 1, 15, and 22 postinjection and corresponding histology. In Figure 7*A*, signal loss is visible in the inguinal node at day 1. In Figure 7*B*, a representative FIESTA image of a mouse at day 15 postinjection shows a heterogeneous pattern of signal loss within the developing tumor that is more than twice the normal size of the inguinal node. In Figure 7*C*, a representative FIESTA image of a mouse that received an injection of *unlabeled* cells is shown at day 15; the unlabeled cells were injected on the opposite side. Note that signal loss is not observed in tumors developing from unlabeled melanoma cells (*arrow*). In Figure 7*D*, a representative FIESTA image of a mouse at day 22 postinjection shows a very large tumor with a heterogeneous pattern of signal loss and hyperintensity. Some banding artifacts are visible (*black arrows*),

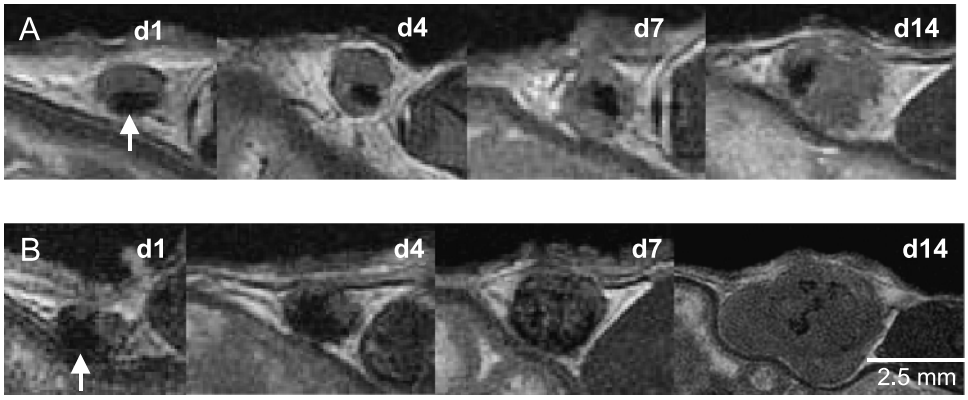

Figure 6. Coronal *in vivo* FIESTA images of mouse inguinal lymph nodes (cropped and enlarged). Monitoring the growth of tumors from iron-labeled melanoma cells postinjected with (A, top row) 1000 or (B, bottom row) 10,000 cells. The signal loss caused by the iron-labeled melanoma cells is evident at day 1 postinjection (arrows) and persists as the tumor develops between days 1 and 14 postinjection.

at the edge of the mouse body, caused by nonoptimal loading of the radiofrequency coil with the mouse, now with a large tumor. Perls' Prussian blue–stained sections of the node at day 1 indicate the presence of iron-labeled cells within the node parenchyma (Figure 7*E*). Perls' Prussian blue–stained section of the nodal tumor developing at day 15 shows that iron can still be detected in some cells at this late time point (Figure 7*F*). S100, shown here for the day 15 example with unlabeled cells, was useful for identifying melanoma cells within the tumor cell mass (Figure 7*G*, *diffuse cytoplasmic brown staining*). In Figure 7*H*, H&E staining shows a tumor at day 22, depicting bands

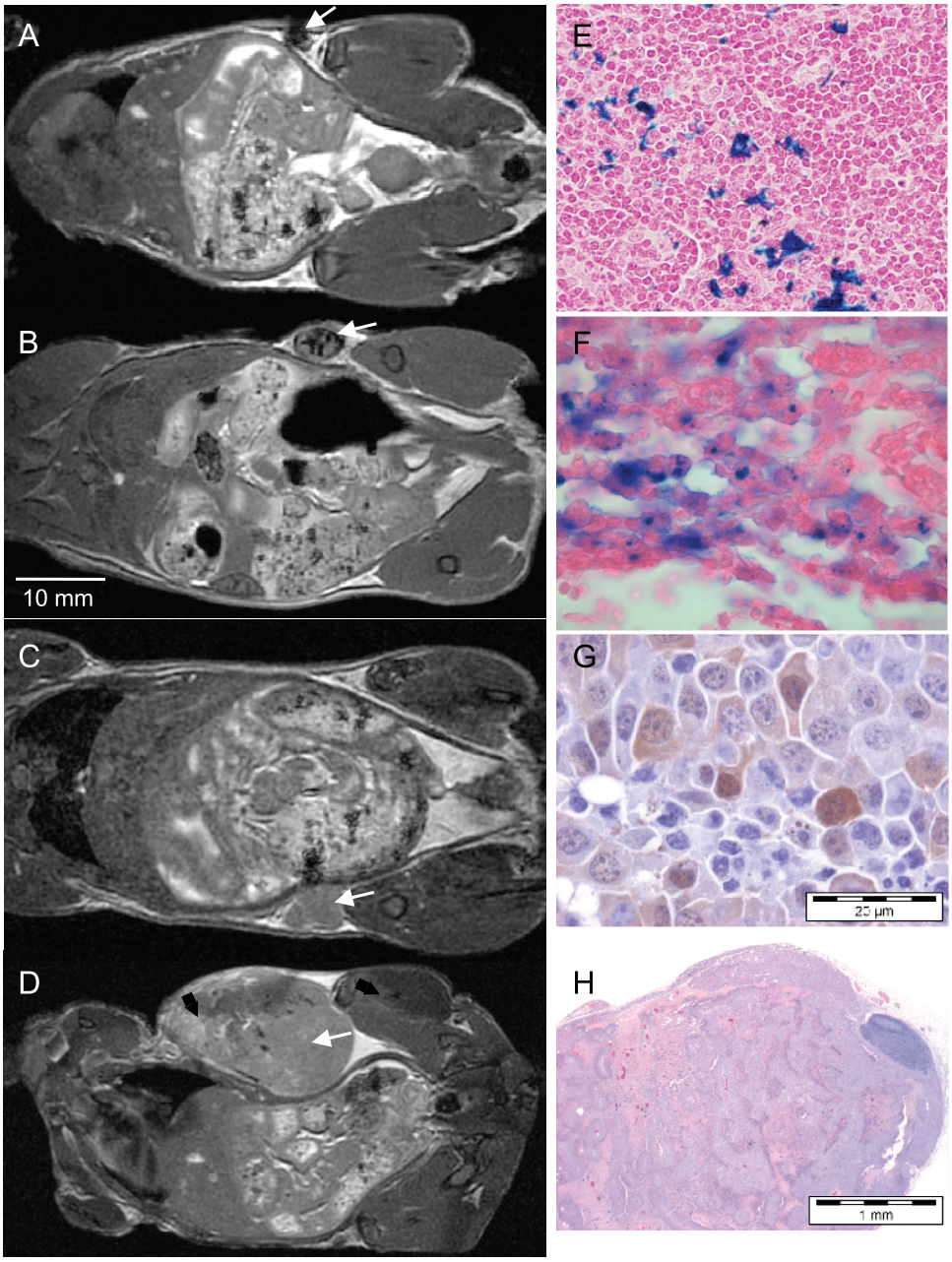

Figure 7. Images of mice, injected with 10,000 cells, and imaged on (A) day 1, (B, C) 15, or (D) 22 postinjection before sacrifice for histological analysis. (A) Coronal FIESTA image of mouse injected with iron-labeled cells shows the region of signal loss on one side of the node on day 1 (arrow). On dissection, the node had a small focal dark spot on one side. (B) Coronal FIESTA image of mouse injected with iron-labeled cells shows a distinct pattern of signal loss within the developing nodal tumor on day 15 (arrow). The node is approximately twice the normal size. (C) Coronal FIESTA image of mouse injected with unlabeled cells shows a homogeneous signal with no signal loss within the developing intranodal tumor on day 15 (arrow). (D) Coronal FIESTA image of mouse injected with iron-labeled cells shows a heterogeneous signal within the tumor on day 22 (arrow) with regions of signal hyperintensity. (E) PPB staining of the node from day 1 shows iron-positive cells invading the node tissue (original magnification, ×10). (F) PPB staining of the node from day 15 (image in B) shows iron-positive cells invading the node tissue (original magnification, ×40). (G) S100 staining of the tumor in C shows positive melanoma cells within the tumor cell mass appearing as regions of diffuse, brown cytoplasmic staining (original magnification, ×40). (H) H&E staining shows that, at day 22, the tumor exhibited bands of necrotic tumor cells, with surviving tumor cells centered around the vascular structures, suggesting that ischemia was the mechanism driving cell death (original magnification, ×4).

of necrotic tumor cells, with surviving tumor cells centered around vascular structures, suggesting that ischemia was the mechanism driving cell death.

Although only the inguinal lymph nodes were imaged in this study, other nodes were examined at dissection. In 3 of 15 mice injected with 10,000 labeled cells, the brown pigmentation of melanoma cells was detected on the ipsilateral axillary node, indicating the occurrence of metastatic trafficking and progression.

Discussion

Many primary malignancies spread through the lymphatic system. The presence of metastases in sentinel lymph nodes and other nodes within the regional bed provide clinically important information for tumor staging, choice of treatment, and prediction of patient outcomes [32,33]. Tumor cells passing through, or residing in, lymph nodes may provide a reservoir of cells leading to distant, lethal metastases. The clinical significance of micrometastases in the lymph is a hotly debated topic, but an improved understanding of the lymphatic spread of cancer remains important for improving cancer survival. Advances toward understanding the interactions between tumor cells and the lymphatic system have been, in part, limited by the lack of suitable noninvasive assays and experimental models.

Recently, we developed MRI hardware and optimized pulse sequence technology to allow the detection of single cells, labeled with MPIO particles, *in vivo* in mouse brain [34,35]. The establishment of this single-cell detection sensitivity coupled with an ability to produce images at high spatial resolution (~100-μm voxel size in each of three dimensions) makes cellular MRI a strong *in vivo* imaging modality for studying cancer metastasis. Here, we report the first application of *in vivo* cellular MRI technology for the direct detection of metastatic melanoma cells in the lymphatic system. We have demonstrated that high-resolution MRI can be used to reliably image the lymph nodes in a mouse model of regional malignant disease and to detect and monitor prelabeled tumor cells within the lymph nodes at levels leading to progressive disease.

The direct intranodal injection of metastatic melanoma cells provides a model system for investigating regional tumor growth, cellular trafficking, and micrometastatic progression. Although the direct implantation of cells into the inguinal lymph node bypasses the normal steps in the progression of metastasis, this model had certain benefits. One advantage is that it creates a more reproducible research model. By injecting a known number of cells into a lymph node, we ensure that each animal is starting from a similar challenge state. This is important when comparing animals in an imaging study. Because natural metastatic progression is more varied, we would initially require many additional challenged animals to generate enough at a similar stage for a single study. So by using direct nodal injections, we increase repeatability and reduce animal use in each study.

Before this study, we compared the intranodal injection of melanoma cells to a subcutaneous injection of cells into the flank, a more commonly used model that is generally considered to better represent spontaneous metastasis. The two models produced similar results. Briefly, six mice received a subcutaneous injection of 10,000 B16F10 cells and six mice received an injection of 10,000 B16F10 cells directly into the inguinal node. Tumors grew at the site of implantation in all mice. Metastasis to regional lymph nodes was observed (on day 28 postmortem) in three of six mice with the subcutaneous injections and in four of six mice with the intranodal injections. The average weight of the nodal tumors was 2.42 g, and the average weight of the subcutaneous tumors was 4.99 g. The imaging results were also similar; that is, iron-labeled cells were detected at the implantation site and signal loss became dispersed in growing tumors with time. The problem with the subcutaneous model was that tumors grew faster and became larger within a shorter time frame. The large subcutaneous tumors protruded from the body and sometimes made it difficult to position the mice within the radiofrequency coil. Mice had to be sacrificed earlier, which may not allow enough time for metastasis to occur or for longer-term monitoring in future studies. For these reasons, we selected the intranodal model.

Much of our current understanding of the metastatic process has come from the use of various *in vivo* imaging modalities that have provided us with the ability to visualize different steps in the metastatic process. Each modality has its strengths but also its limitations imposed by technological constraints. Optical techniques, such as bioluminescence imaging, while sensitive to small numbers of cells (detection limits of 1000 cells), are limited by the penetration of light through optically opaque tissues and are also seriously limited by spatial resolution, even in mice [36]. With surgical exposure, optical microscopic methodologies such as intravital video microscopy can achieve single-cell detection; however, the small fields of view of this technique can only allow examination of a small fraction of the overall target organ, and individual animals can typically only be followed for short periods of time, e.g., hours [23]. Computed tomography can produce images of the entire mouse anatomy at high spatial resolution (in the order of ~50 μm) but has poor soft tissue contrast, and there are no current computed tomography contrast agents that allow cell tracking [37]. Positron emission tomography and single-photon emission computed tomography are high-sensitivity imaging techniques capable of detecting small numbers of cells [37] (hundreds) within the entire organism but have low spatial resolution, making it difficult to differentiate small groups of cells within target organs. High-frequency US (20 to 60 MHz) can produce images of high spatial (~50 μm) and temporal resolution, but the detection of tumors by US is limited by the penetration of high-frequency sound waves in tissue and by bone/air–tissue interfaces that are not echogenically accessible [23].

Standard lymphatic MRI is limited to the detection of nodes that are enlarged and/or irregular [38]. This is a pitfall, because micrometastases can often be found in normal-sized and shaped nodes and because things other than malignancy may cause enlarged nodes. The use of contrast agents for MRI has improved visualization of nodes. Both iron- and gadolinium (Gad)-based contrast agents are currently undergoing testing to increase the use of this imaging modality for lymph diagnoses [39,40]. Iron oxide nanoparticles have been used to detect metastases in lymph nodes since the late 1990s, and some agents (i.e., USPIO) are in clinical trial [41,42]. Iron-based agents are administered intravenously and slowly accumulate in the lymph-node macrophages. In malignant nodes, the normal tissue appears with low signal and the metastatic tissue appears unchanged. False negatives may result if there is enough normal tissue taking up iron to cause the whole node to appear black because of blooming, effectively hiding metastatic tissue. In addition, reactive nodes containing primarily lymphocytes, which do not take up iron, may result in false positives [38]. Gad-based agents have been used to improve the ability to visualize lymph nodes [43]. With Gad-based agents, normal node tissue appears bright in the images, whereas metastatic tissue remains unchanged [38]. Neither iron- nor Gad-based agents provide

direct visualization of cancer cells in nodes; both methods work by changing the signal intensity of normal nodal tissue.

Our novel approach to cellular MRI allowed for cell detection of as few as 100 MPIO-labeled cells within the lymph node, with injections of larger cell numbers producing increasingly obvious regions of signal void. This success in detecting small numbers of MPIO-labeled cells within the mouse lymph nodes *in vivo* is the result of achieving simultaneously high-resolution and high SNR images of the mouse body. A significant advancement that has allowed us to do this has been the implementation and optimization of the FIESTA pulse sequence for this microimaging application. This pulse sequence is extremely sensitive to the presence of cellularly compartmentalized iron, but possesses high SNR efficiency. These two characteristics confer an advantage over the more conventional T_2- and T_2*-weighted pulse sequences used for imaging iron-labeled cells by most other groups [44–47]. In addition to pulse sequence optimization, improvements in MR hardware, specifically our implementation of high-performance gradient coil technology, is a significant factor in our successful demonstration of cell sensitivity. The higher intrinsic SNR and resolution afforded by these optimized pulse sequence and hardware components are the chief contributing factors that have allowed us to achieve low-level *in vivo* cell detection in the lymphatics while still using low field strengths that are clinically applicable.

Often, it is desired not only to detect small numbers of cells but also to track their fate over time. A potential limitation of the *in vitro* labeling and tracking schemes is the loss of cell detection that may be expected to occur with cell division and dilution of the iron label. Our *in vitro* studies performed to assess the iron concentration in dividing cells showed that intracellular iron disappears from dividing B16F10 cells within 5 days after labeling in culture. This agrees with previous *in vitro* studies, which showed that cell division and metabolism of biodegradable SPIO agents leads to the loss of sufficient iron for HeLa cell detection within five to eight generations [48]. Despite what has been observed *in vitro*, our results show that image contrast due to MPIO-labeled cells persists for as long as 22 days in developing melanomas. When 10,000 iron-labeled cells were implanted, images at day 1 showed a large focal region of signal loss. Over time, this focal signal loss became dispersed throughout the developing tumor. In the last scan, on day 22, signal loss persisted within the tumor. It is unlikely that the regions of signal loss dispersed throughout the large tumors represent necrosis because signal loss was not observed in tumors when unlabeled cells were implanted. In addition, our pathology report indicated that, when there was tumor necrosis, there was also hemorrhage. We have previously shown that hemorrhagic necrosis appears with increased signal intensity on FIESTA images [49]. Signal hyperintensity, likely due to necrosis and edema, was observed in FIESTA images of the larger tumors in mice imaged at day 22 postinjection. This persistent contrast may indicate heterogeneity in cell proliferation, division of the magnetic particles between dividing cells, and/or cell death within the tumor and may suggest an advantage for the use of the biologically inert MPIO for cellular MRI of rapidly dividing cells.

We observed other interesting examples of the persistence of signal loss. When 100 iron-labeled cells were implanted, the pattern of signal loss was consistent over time. In these cases, there was no tumor growth, so it is likely that this represents the presence of iron-labeled, nonproliferative cells in the node. In one case, when 1000 iron-labeled cells were implanted, the focal region of signal loss observed on day 1 appeared unchanged as the node clearly expanded around it. The simplest interpretation of this observation might be that the iron-labeled cells remain in the original site of implantation while unlabeled cells proliferate. We know that the MPIO does not prevent or impair cancer cell division, from routine cell proliferation assays (data not shown). An alternative interpretation is that only a very small population of the implanted cells proliferate to form the tumor cell mass. This is plausible because tumor growth with this low cell number is rather unpredictable. In half of the mice, implanted with 1000 iron-labeled cells, no tumors were developed at all. It is well known that in experimental models, the number of cancer cells injected or implanted is a major factor in tumor incidence and growth rates. In summary, our data show that, in a complex *in vivo* tumor system, the contrast from iron-labeled cells can persist for much longer than would be predicted by *in vitro* cell division assays.

One remaining challenge is the ability to access and label tumor cells *in situ* within lymphatics and other organs. Our future studies will investigate a double-contrast approach by combining iron-based contrast agents for labeling cancer cells (*negative contrast*) with positive contrast agents for enhancing the lymphatic tissues and vessels.

Acknowledgments

We thank Andrew Alejski and Brian Rutt for technical support and Soha Ramadan for assistance with editing the manuscript.

References

[1] Ries LAG, Eisner MP, Kosary CL, Hankey BF, Miller BA, Clegg L, Mariotto A, Fay MP, Feuer EJ, and Edwards BK (2003). SEER Cancer Statistics Review, 1975–2000. Bethesda, MD National Cancer Institute [Tables XVI-1-9].

[2] Markovic SN, Erickson LA, Rao RD, Weenig RH, Pockaj BA, Bardia A, Vachon CM, Schild SE, McWilliams RR, Hand JL, et al. (2007). Melanoma Study Group of Mayo Clinic Cancer Center. Malignant melanoma in the 21st century: Part 1. Epidemiology, risk factors, screening, prevention, and diagnosis. *Mayo Clin Proc* **82**, 364–380.

[3] Lucas R, McMichael T, Smith W, and Armstrong B (2006). Solar ultraviolet radiation: global burden of disease from solar ultraviolet radiation. *Environmental Burden of Disease Series, No. 13* Geneva, Switzerland World Health Organization.

[4] Miller AJ and Mihm MC Jr (2006). Melanoma. *N Engl J Med* **355**, 51–65.

[5] Swanson NA, Lee KK, Gorman A, and Lee HN (2002). Biopsy techniques. Diagnosis of melanoma. *Dermatol Clin* **20**, 677–680.

[6] Homsi J, Kashani-Sabet M, Messina JL, and Daud A (2005). Cutaneous melanoma: prognostic factors. *Cancer Control* **12**, 223–229.

[7] Markovic SN, Erickson LA, Rao RD, Weenig RH, Pockaj BA, Bardia A, Vachon CM, Schild SE, McWilliams RR, Hand JL, Melanoma Study Group of Mayo Clinic Cancer Center, et al. (2007). Malignant melanoma in the 21st century: Part 2. Staging, prognosis, and treatment. *Mayo Clin Proc* **82**, 490–513.

[8] Balch CM, Buzaid AC, Soong SJ, Atkins MB, Cascinelli N, Coit DG, Fleming ID, Gershenwald JE, Houghton A Jr, Kirkwood JM, et al. (2001). Final version of the American Joint Committee on Cancer staging system for cutaneous melanoma. *J Clin Oncol* **19**, 3635–3648.

[9] Chambers AF, Groom AC, and MacDonald IC (2002). Dissemination and growth of cancer cells in metastatic sites. *Nat Rev Cancer* **2**, 563–572.

[10] Vantyghem SA, Postenka CO, and Chambers AF (2003). Estrous cycle influences organ-specific metastasis of B16F10 melanoma cells. *Cancer Res* **63**, 4763–4765.

[11] Yan WH, Lin AF, Chang CC, and Ferrone S (2005). Induction of HLA-G expression in a melanoma cell line OCM-1A following the treatment with 5-aza-2′-deoxycytidine. *Cell Res* **15**, 523–531.

[12] Maeshima S, Yamada T, Kiyokane K, and Mori H (2007). Establishment and characterization of a cell line (DEOC-1) originating from a human malignant melanoma of the skin. *Hum Cell* **20**, 23–38.

[13] Jenkins DE, Hornig YS, Oei Y, Dusich J, and Purchio T (2005). Bioluminescent human breast cancer cell lines that permit rapid and sensitive *in vivo* detection of mammary tumors and multiple metastases in immune deficient mice. *Breast Cancer Res* **7**, R444–R454.

[14] Chambers AF, MacDonald IC, Schmidt EE, Koop S, Morris VL, Khokha R, and Groom AC (1995). Steps in tumor metastasis: new concepts from intravital videomicroscopy. *Cancer Metastasis Rev* **14**, 279–301.

[15] Kennel SJ, Davis IA, Branning J, Pan H, Kabalka GW, and Paulus MJ (2000). High resolution computed tomography and MRI for monitoring lung tumor growth in mice undergoing radioimmunotherapy: correlation with histology. *Med Phys* **27**, 1101–1107.

[16] Graham KC, Wirtzfeld LA, MacKenzie LT, Postenka CO, Groom AC, MacDonald IC, Fenster A, Lacefield JC, and Chambers AF (2005). Three-dimensional high-frequency ultrasound imaging for longitudinal evaluation of liver metastases in preclinical models. *Cancer Res* **65**, 5231–5237.

[17] Gambhir SS (2002). Molecular imaging of cancer with positron emission tomography. *Nat Rev Cancer* **2**, 683–693.

[18] Blankenberg FG, Katsikis PD, Tait JF, Davis RE, Naumovski L, Ohtsuki K, Kopiwoda S, Abrams MJ, Darkes M, Robbins RC, et al. (1998). *In vivo* detection and imaging of phosphatidylserine expression during programmed cell death. *Proc Natl Acad Sci USA* **95**, 6349–6354.

[19] Weissleder R (2002). Scaling down imaging: molecular mapping of cancer in mice. *Nat Rev Cancer* **2**, 11–18.

[20] Benveniste H, Kim K, Zhang L, and Johnson GA (2000). Magnetic resonance microscopy of the C57BL mouse brain. *Neuroimage* **11**, 601–611.

[21] Petiet A, Hedlund L, and Johnson GA (2007). Staining methods for magnetic resonance microscopy of the rat fetus. *J Magn Reson Imaging* **25**, 1192–1198.

[22] Modo M, Hoehn M, and Bulte JW (2005). Cellular MR imaging. *Mol Imaging* **4**, 143–164.

[23] Arbab AS, Liu W, and Frank JA (2006). Cellular magnetic resonance imaging: current status and future prospects. *Expert Rev Med Devices* **3**, 427–439.

[24] Corot C, Robert P, Idee JM, and Port M (2006). Recent advances in iron oxide nanocrystal technology for medical imaging. *Adv Drug Deliv Rev* **58**, 1471–1504.

[25] Bulte JW and Kraitchman DL (2004). Iron oxide MR contrast agents for molecular and cellular imaging. *NMR Biomed* **17**, 484–499.

[26] Thorek DL, Chen AK, Czupryna J, and Tsourkas A (2006). Superparamagnetic iron oxide nanoparticle probes for molecular imaging. *Ann Biomed Eng* **34**, 23–38.

[27] Frank JA, Anderson SA, Kalsih H, Jordan EK, Lewis BK, Yocum GT, and Arbab AS (2004). Methods for magnetically labeling stem and other cells for detection by *in vivo* magnetic resonance imaging. *Cytotherapy* **6**, 621–625.

[28] Suzuki Y, Zhang S, Kundu P, Yeung AC, Robbins RC, and Yang PC (2007). *In vitro* comparison of the biological effects of three transfection methods for magnetically labeling mouse embryonic stem cells with ferumoxides. *Magn Reson Med* **57**, 1173–1179.

[29] Hinds KA, Hill JM, Shapiro EM, Laukkanen MO, Silva AC, Combs CA, Varney TR, Balaban RS, Koretsky AP, and Dunbar CE (2003). Highly efficient endosomal labeling of progenitor and stem cells with large magnetic particles allows magnetic resonance imaging of single cells. *Blood* **102**, 867–872.

[30] Shapiro EM, Skrtic S, Sharer K, Hill JM, Dunbar CE, and Koretsky AP (2004). MRI detection of single particles for cellular imaging. *Proc Natl Acad Sci USA* **101**, 10901–10906.

[31] Fidler IJ (1973). Selection of successive tumour lines for metastasis. *Nat New Biol* **242**, 148–149.

[32] Cserni G (2007). Pathological evaluation of sentinel lymph nodes. *Surg Oncol Clin N Am* **16**, 17–34.

[33] Blaheta HJ, Ellwanger U, Schittek B, Sotlar K, MacZey E, Breuninger H, Thelen MH, Bueltmann B, Rassner G, and Garbe C (2000). Examination of regional lymph nodes by sentinel node biopsy and molecular analysis provides new staging facilities in primary cutaneous melanoma. *J Invest Dermatol* **114**, 637–642.

[34] Heyn C, Ronald JA, Mackenzie LT, MacDonald IC, Chambers AF, Rutt BK, and Foster PJ (2006). *In vivo* magnetic resonance imaging of single cells in mouse brain with optical validation. *Magn Reson Med* **55**, 23–29.

[35] Heyn C, Ronald JA, Ramadan SS, Snir JA, Barry AM, MacKenzie LT, Mikulis DJ, Palmieri D, Bronder JL, Steeg PS, et al. (2006). *In vivo* MRI of cancer cell fate at the single-cell level in a mouse model of breast cancer metastasis to the brain. *Magn Reson Med* **56**, 1001–1010.

[36] Troy T, Jekic-McMullen D, Sambucetti L, and Rice B (2004). Quantitative comparison of the sensitivity of detection of fluorescent and bioluminescent reporters in animal models. *Mol Imaging* **3**, 9–23.

[37] Seevinck PR, Seppenwoolde JH, de Wit TC, Nijsen JF, Beekman FJ, van Het Schip AD, and Bakker CJ (2007). Factors affecting the sensitivity and detection limits of MRI, CT, and SPECT for multimodal diagnostic and therapeutic agents. *Anticancer Agents Med Chem* **7**, 317–334.

[38] Barrett T, Choyke PL, and Kobayashi H (2006). Imaging of the lymphatic system: new horizons. *Contrast Media Mol Imaging* **6**, 230–245.

[39] Kobayashi H, Kawamoto S, Brechbiel MW, Bernardo M, Sato N, Waldmann TA, Tagaya Y, and Choyke PL (2005). Detection of lymph node involvement in hematologic malignancies using micromagnetic resonance lymphangiography with a gadolinium-labeled dendrimer nanoparticle. *Neoplasia* **11**, 984–991.

[40] Moore A, Weissleder R, and Bogdanov A Jr (1997). Uptake of dextran-coated monocrystalline iron oxides in tumor cells and macrophages. *J Magn Reson Imaging* **6**, 1140–1145.

[41] Weissleder R, Cheng HC, Bogdanova A, and Bogdanov A Jr (1997). Magnetically labeled cells can be detected by MR imaging. *J Magn Reson Imaging* **1**, 258–263.

[42] Harisinghani MG, Barentsz J, Hahn PF, Deserno WM, Tabatabaei S, van de Kaa CH, de la Rosette J, and Weissleder R (2003). Noninvasive detection of clinically occult lymph-node metastases in prostate cancer. *N Engl J Med* **25**, 2491–2499.

[43] Choi SH, Han MH, Moon WK, Son KR, Won J-K, Kim J-H, Kwon BJ, Na DG, Weinmann H-J, and Chang K-H (2006). Cervical lymph node metastases: MR imaging of gadofluorine M and monocrystalline iron oxide nanoparticle-47 in a rabbit model of head and neck cancer. *Radiology* **241**, 753–762.

[44] Wu YL, Ye Q, Foley LM, Hitchens TK, Sato K, Williams JB, and Ho C (2006). *In situ* labeling of immune cells with iron oxide particles: an approach to detect organ rejection by cellular MRI. *Proc Natl Acad Sci USA* **103**, 1852–1857.

[45] Ahrens ET, Feili-Hariri M, Xu H, Genove G, and Morel PA (2003). Receptor-mediated endocytosis of iron-oxide particles provides efficient labeling of dendritic cells for *in vivo* MR imaging. *Magn Reson Med* **49**, 1006–1013.

[46] Wadghiri YZ, Sigurdsson EM, Wisniewski T, and Turnbull DH (2005). Magnetic resonance imaging of amyloid plaques in transgenic mice. *Methods Mol Biol* **299**, 365–379.

[47] Medarova Z, Pham W, Farrar C, Petkova V, and Moore A (2007). *In vivo* imaging of siRNA delivery and silencing in tumors. *Nat Med* **13**, 372–377.

[48] Arbab AS, Bashaw LA, Miller BR, Jordan EK, Lewis BK, Kalish H, and Frank JA (2003). Characterization of biophysical and metabolic properties of cells labeled with superparamagnetic iron oxide nanoparticles and transfection agent for cellular MR imaging. *Radiology* **229**, 838–846.

[49] Dunn EA, Weaver LC, Dekaban GA, and Foster PJ (2005). Cellular imaging of inflammation after experimental spinal cord injury. *Mol Imaging* **4**, 1–10.